ISTITUTO NAZIONALE DI FISICA NUCLEARE

Sezione di Trieste

INFN/AE-97/29

June 27, 1997

G. Barbiellini and M. Zalateu

EXPERIMENTAL MEASUREMENTS OF THE ANTIMATTER COMPONENT IN COSMIC RAYS

SIS - Pubblicazioni
Laboratori Nazionali di Frascati

EXPERIMENTAL MEASUREMENTS OF THE ANTIMATTER COMPONENT IN COSMIC RAYS.

Presented by Guido Barbiellini
final version by Guido Barbiellini and Massimo Zalateu
I.N.F.N. Trieste
Trieste University, Trieste, Italy

ABSTRACT

The antimatter component of Cosmic Ray flux is mainly due to secondary production from reactions of the primary proton flux on the galactic interstellar medium (ISM). Search for other sources of antimatter as Primordial Black Hole (PBH) evaporation, dark matter decay or annihilation or from antiparticles leakage from far away antigalaxies are of deep interest.

In this lecture the present experimental situation on antimatter search from balloon flights experiments are presented.

The near future experiment are illustrated (long duration balloon flights) the very long term data taking detectors to be sent in space are also briefly reviewed.

Introduction

The world in which we live and the part of world we are able to probe with matter seem to be consistent, at the present average temperature, of being composed mainly of the light quarks u and d, and of electrons. These basic component are bounded together by the quanta of the strong and electroweek interactions.

The fantaquantities of $\overline{u}$, $\overline{d}$ and e^+ are found at certain given time and in few places in our planets, for istance you can find antiproton ($\overline{p}$) or positron (e^+) at CERN (Geneva), Fermilab (Chicago), SLAC Stanford and few more place in Japan, in USA and Europe.

In the Cosmic Rays of our galaxy there is a sizeble amount of $\overline{p}$ and e^+ ($\overline{p}$ /p$\sim$ 10^{-4}; e^+ /e^- $\sim 10^{-1}$). The amount of known antimatter in our galaxy is compatible with the production mechanism (1) and (2) from the interactions of the primary proton on the interstellar medium (ISM).

(1) $pp \rightarrow \overline{p} + X$ (2) $pp \rightarrow \pi + Y$

$\hookrightarrow \mu^{\pm} + \nu_{\mu}$

$\hookrightarrow e^{\pm} + \nu_e + \nu_{\mu}$

If the presence of antimatter in our and other galaxies is only that coming from reactions (1) and (2), some time between the Big Bang and the 100 GeV temperature a not well defined interaction has introduced an asymmetry in the baryons as well in the leptons.

The search for antimatter in the cosmic ray flux is motivated by the following reason:

1. Search for predictable sources of positron (e^+) and antiproton ($\overline{p}$) to test ipothesys of the models, Galactic interstellar matter and confining mechanism.
2. Search for possible excess of e^+ and $\overline{p}$ from possible exotic sources: Primordial Black Hole (PBH) evaporation, Supersymmetric dark matter candidates annichilation, or decay.

1 The Discovery of Cosmic Rays.

The muons are part of the natural background radiation which was discovered early this century. It was assumed to come from the ground with the intensity therefore decreasing at higher altitudes. It was a great surprise when Victor Hess in his historical balloon flight (Figure 1) of 1912 discovered that the intensity increased with the altitude. Hess used an electroscope to measure the ionization as a function

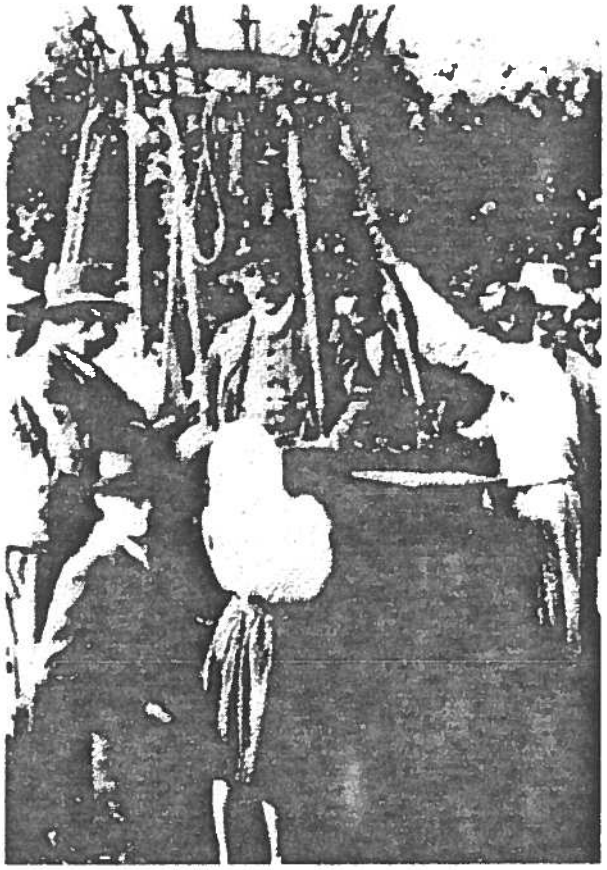

Figure 1: Victor F. Hess in the balloon after one of the first successful flights in which the cosmic radiation was discovered.

of altitude (Results from different electroscope measurement are reported in Table 1). He concluded that the increase colud best be explained by penetrating radiation incident on the atmosphere from above. It took some years before this conclusion was generally accepted.

In the tradition of Hess, many more balloon flights have been dedicated to cosmic ray measurements. Studies have been made of the energy spectra and composition. The dominant part (90%) of the cosmic radiation reaching the Earth comprises of protons. Of the remaining part, 4% is helium, 2% carbon and oxigen, and rest are

Table 1:

Altitude (km)	Difference between observed ionization and that at sea-level (ions cm^{-3})
1	-1.5
2	+1.2
3	+4.2
4	+8.8
5	+16.9
6	+28.7
7	+44.2
8	+61.3
9	+80.4

heavier elements with a large fraction of iron (if the fluxes are given as particles per GeV per nucleon). The proportions of these components are relatively constant with energy. Their spectra are described by an inverse power law in energy and the differential flux (dN/dE). Figure 2 shows proton cosmic rays energy spectra measured by different flight of the Japan-USA mission BESS.

1.1 Sources of the antimatter in Cosmic Rays (C.R.)

The predictable amount of antimatter in the C.R. is of secoundary production from the proton C.R. (see Figure 2) colliding with the Interstellar Medium of our Galaxy (ISM) and producing secondary pions and antiproton according the reactions:

$$p_{CR} + p_{ISM} \rightarrow \pi^{\pm} + X \qquad\qquad p_{CR} + p_{ISM} \rightarrow \overline{p} + Y \tag{1}$$

where X and Y are a system of pion and baryons. The pion decay (see introduction (2)) induce the positron (e^+) component of the C.R.. The main uncertitude on the prediction of the absolute flux of positron (e^+) and antiproton ($\overline{p}$) comes from the equivalent amount of ISM seen by the primary protons in the containement time of the secondary e^+ and $\overline{p}$.

Antimatter is also interesting from the standpoint of cosmology and elementary particle physics. Evidence of primary (not produced in a p-p interaction in the interstellar matter) antiproton component from an extragalactic source would provide the first evidence for large quantities of antimatter in the Universe. Futhermore, a primary $\overline{p}$ and e^+ component could also arise from annihilation of dark matter or evaporation of primordial black holes.

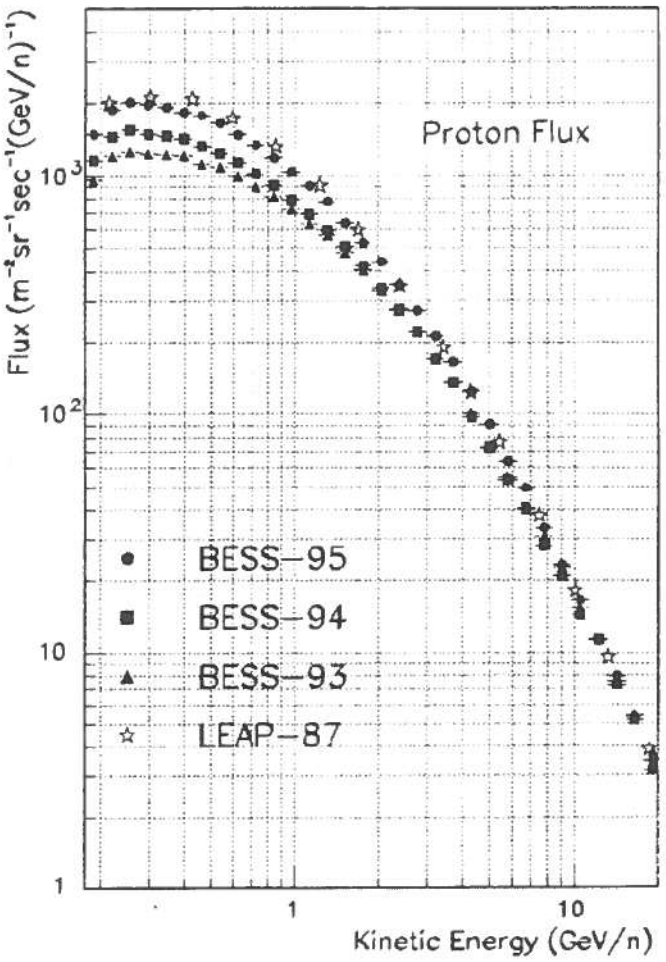

Figure 2: Proton flux measurements in BESS-93, 94 and 95 compared with the LEAP experiment, 1987.

2 The Cosmic Ray positron component.

Measurement of the e^+ component of C.R. started in the early seventy (Fanselow et al. 1969, Daugherty et al. 1975). The major problems associated with the balloon borne positron measurement are:

i) the e^+ discrimination against the main proton component

ii) the correction for e^+ produced in the residual atmosphere and on the top of the balloon.

The very recent data on e^+ in C.R. collected by the CAPRICE collaboration are reported in the following.

The positron to electron ratio in the cosmic radiation have been measured over more than one decade in energy from 0.85 to 14 GeV, using the NMSU-Wizard/CAPRICE balloon borne magnet spectrometer. The spectrometer uses a

solid radiator RICH detector and a silicon-tungsten calorimeter for particle identification. The proton rejection factor of the two instruments combined is better than 2×10^{-6} between 0.6 and 3 GV/c dropping to 6×10^{-5} at 5 GV/c and 10^{-4} at 10 GV/c. The data was collected during 23 hours at a mean residual atmosphere of 4.0 g/cm^2. From a total of 2756 well identified e^- and 498 e^+ the positron fraction $R = e^+ /(e^+ + e^-)$ as a function of energy has benn measured with small errors from 0.85 GeV to 14 GeV for the first time. The energy dependent behaviour of R is consistent with the simple leaky box model. The positron fraction in the upper energy bins are in agreement with the latest high energy measurements.

2.1 Detector system

Figure 3 shows the NMSU-Wizard/CAPRICE spectrometer that was flown from Lynn Lake, Manitoba, Canada on August 8, 1994. From top to bottom it includes a RICH detector (figure 4), a time-of-flight (ToF) system, a magnet spectrometer of multiwire proportional chmbers (MWPC) and drift chambers (DC) and a silicon-tungsten imaging calorimeter.

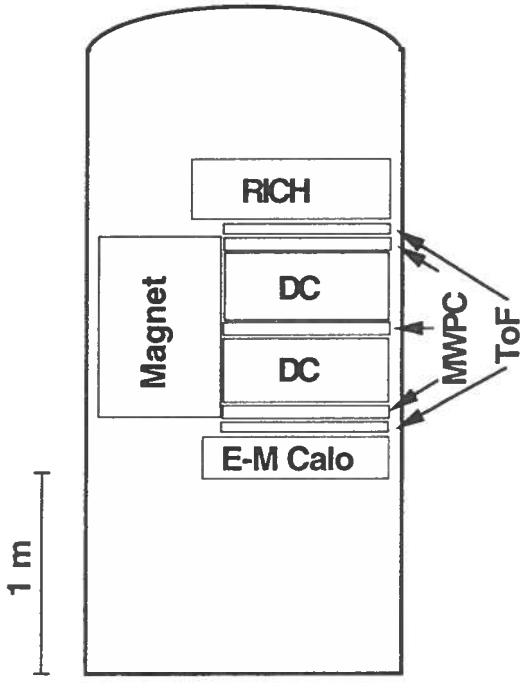

Figure 3: A schematic view of the CAPRICE gondola.

The RICH detector (Carlson et al, 1994, Carlson et al, 1995), with a thresold Lorentz factor of 1.5, uses a solid NaF radiator and a photosensitive MWPC with pad readout to detect the Cherenkov light image. It was used to measure the velocity of the particles. The ToF system consists of two layers of plastic scintillators,

one above and one below the tracking stack. It was used to give a trigger as well as to measure the time-of-flight and dE/dx losses of the particles. The magnet spectrometer (Golden et al. 1991, Hof et al. 1994) measures the rigidity of the particle with an average maximum detectable rigidity of 200 GV/c. finally, the electromagnetic calorimeter (Bocciolini et al. 1991) is composed of eight planes of double-sided silicon strip detectors interleaved with seven layers of tungsten converters (each one radiation length thick). The silicon strips are placed perpendicular to each other, giving the energy deposited in each strip. Moreover, this imaging device provides information on the longitudinal as well as the lateral profile of the cascade.

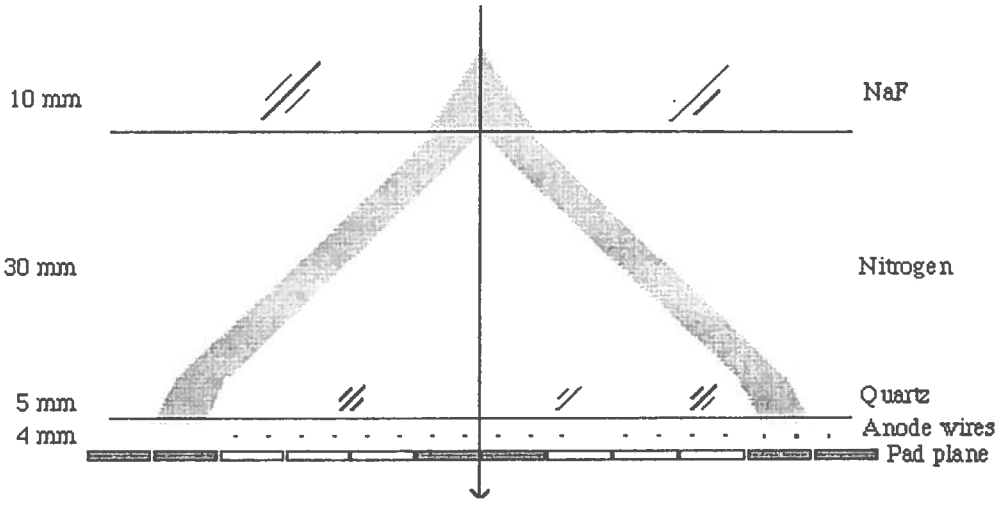

Figure 4: A schematic view of the NaF-RICH detector.

2.2 Data analysis

During the 23 hour long flight more than six million events were recorded at a mean residual atmosphere of 4.0 g/cm^2. Electrons and positrons were selected in the rigidity range between 0.6 and 10 GV/c. Events with a single track having an acceptable chi-square in the tracking of the spectrometer were accepted. The selected singly charged particles give a signal corresponding to less than 1.7 mips (minimum ionizing particles) in the top ToF scintillator. Albedo events were rejected using both the ToF and the RICH. An electron sample was selected as particles with negative deflection, $\beta = 1$ as detected by the RICH and an electromagnetic shower in the calorimeter.

The cuts imposed on the calorimeter to identify electromagnetic showers have a logarithmic dependence on rigidity and are based on (a) results from an experiment using particle beams at CERN (Bocciolini et al. 1993), (b) simulations and (c)

experience gained from a previous flight with the same instrument (Golden et al. 1996). An electromagnetic shower is characterized by a narrow shower with most of the energy deposited inside 4 Molière radii around the track. Additional cuts based on the total detected energy, which should match the measured momentum, and on the longitudinal and lateral profiles of the shower were applied. A small number of particles emit a bremsstrahlung photon before entering the calorimeter (e.g. in the RICH or the aluminum cover of the gondola) that was detected in the calorimeter as a parallel shower. These double shower events with a single track in the tracking system are clearly electron/positron events and can be used with looser cuts. The detection efficiency of the calorimeter using the above cuts is rigidity dependent increasing from 80% at 0.6 GV/c to 85% above 0.7 GV/c, being constant 85% between 0.7 and 3 GV/c then slowly decreasing to 75% at 10 GV/c.

The RICH was used to measure the velocity (β) of the particles. Due to the high rejection factor of the calorimeter, rather loose cuts were applied on the RICH data in order to maximize the efficiency of selection. Electrons and positrons were selected by the RICH as $\beta = 1$ particles with a well defined Cherenkov light image and a good agreement between the position determined by the RICH and that from the tracking measurement. With these cuts applied, the RICH has a constant detection efficiency of 72% between 0.6 and 5 GV/c. Above 5 GV/c the RICH is not capable of separating protons from positrons and was not used.

The scintillator cut of $\leq$1.7 mip gave an efficiency of 98% for protons, pions and muons. Electrons and positrons can emit bremsstrahlung photons which materialize in or above the top scintillator. These events will be rejected by the cuts applied. The efficiency for electrons and positrons is found to be decreasing from 86% at 0.6 GeV to 81% at 10 GeV due to a small increase in shower multiplicity.

2.3 Results

Table 2 gives the number of electrons and positrons that pass the cuts applied on the RICH, the ToF and the calorimeter. In order to estimate the number of protons which simulate a positron-like cascade in the calorimeter, we selected a proton sample using the RICH and ToF for rigidities less than 1.4 GV/c. In this energy region the RICH acts as a threshold counter and the ToF is able to separate protons from lighter particles. Between 1.4 and 5.0 GV/c the RICH can accurately identify protons. On this proton sample the calorimeter cuts were applied and the surviving protons were used to determine the contamination. The proton contamination was found to be 8×10^{-4} for rigidities between 0.6 and 1.0 GV/c and less than 1×10^{-4} between 1 and 5 GV/c. In the energy region from 5 to 10 GV/c The contamination

is assumed to be the same as that of the bin 3 to 5 GV/c , that is: $(1.1 \pm 0.5) \times 10^{-4}$.

The muon and pion background was estimated using Monte Carlo simulations. The pion contamination was found to be 5×10^{-3} below 1 GV/c and less than 1×10^{-3} between 1 and 5 GV/c. However, the abundance of pions is less than 1×10^{-3} of the protons at this small atmospheric depth and hence the pion contamination is insignificant. The muon contamination was negligible at all rigidities.

The number of protons passing the RICH cuts was estimated using a proton sample selected by the ToF below 1 GV/c, and by the calorimeter above 1 GV/c by requiring an hadronic interaction. The proton contamination in the RICH was found to be 2×10^{-3} between 0.6 and 1 GV/c increasing to 2% at 3 GV/c, 30% at 4 GV/c and 60% at 5 GV/c due to the loose cuts applied. It may be pointed out that the RICH cannot separate muons and pions from electrons and positrons in the energy region of interest in this analysis.

Assuming that the rejection of protons by the RICH and the calorimeter is independent we get a total proton contamination of less than 2×10^{-6} between 0.6 and 3 GV/c increasing to 6×10^{-5} at 5 GV/c and 10^{-4} at 10 GV/c. The rejection factor of the calorimeter and the RICH is high enough to eliminate all proton, pion and muon contamination from the positron sample between 0.6 and 3 GV/c. The proton contamination was found to be 9% and 17% of the positron sample in the rigidity bins 3 to 4 GV/c and 4 to 5 GV/c, respectively. In the rigidity region 5 to 10 GV/c only the calorimeter has been used resulting in a proton contamination of 25% of the selected positron sample. This proton contamination is shown in the parenthesis in Table 2 and was subtracted from the positron sample.

The secondary positrons and electrons, which are produced in the residual atmosphere above the instrument were estimated in the following manner. We first determined the energy spectrum of the negative muons. These muons were identified by requiring minimum ionizing, negative curvature particles, which enter the instrument from the top and undergo no interaction in the calorimeter. The efficiency of selecting these particles was found to be 98.2%. We show in Fig. 5 the observed spectrum (number of particles per unit energy) of muons from 0.8 GeV to 15 GeV. The dotted curve shown in this figure is the calculated spectrum at 4 g/cm^2 of residual atmosphere (Stephens 1981). Note the excellent agreement with data. At the top of the payload (ToP) most secondary electrons and positrons come from decaying muons. We use the normalization constant obtained from the muon spectrum in Fig. 5 to estimate the secondary electron-positron spectra at 4 g/cm^2 (Stephens 1981).

The observed electron and positron spectra were corrected for the efficiencies

Table 2: Summary of electron - positron results.

Energy bin at spectrometer GeV	Observed number of events[a] e^-	e^+	Extrapolated number at ToP[b] e^-	e^+	Atmospheric correction e^-	e^+	Median energy at ToA[c] GeV	$\frac{e^+}{e^+ + e^-}$ at ToA[c]
0.6 - 0.8	396	121	886.4	300.4	125.5	184.8	0.99	0.14 ± 0.03
0.8 - 1.05	415	105	905.7	237.6	67.6	94.6	1.30	0.132 ± 0.021
1.05 - 1.5	554	103	1212.6	212.4	45.9	65.9	1.77	0.113 ± 0.014
1.5 - 2.0	447	65	1040.2	139.2	20	26.6	2.45	0.090 ± 0.016
2.0 - 3.0	455	49	1003.4	88.9	14.8	18.1	3.45	0.076 ± 0.012
3.0 - 5.0	303	28(4)	632.5	49.4	7	8.6	5.37	0.075 ± 0.015
5.0 - 10.0	186	27(7)	414.8	43.9	2.9	3.4	9.56	0.07 ± 0.03

[a]The numbers shown in the brackets are the estimated proton background.

[b]Top of payload.

[c]Top of atmosphere.

and were extrapolated to the top of the payload using bremsstrahlung corrections. These flux values (particles per unit energy) are shown in Fig. 5 as a function of energy. The estimated atmospheric secondary electrons and positrons are also shown by dashed and solid curves, respectively. The number of secondary particles are tabulated in Table 2 along with the extrapolated number of observed electrons and positrons to the top of the payload.

To check the correctness of this procedure, the growth curve of the electrons in the atmosphere from 4 g/cm^2 to 200 g/cm^2 in the energy interval 0.6-0.9 GeV was studied. By normalizing the calculated growth curve (Daniel and Stephens 1974) for 700 MeV electrons over the depth between 30 and 150 g/cm^2, the fraction of secondary electrons turn out to be 13.2±1.9% at 4 g/cm^2. From the Table 2, one can estimate that the fraction of secondary electrons in the energy interval between 0.6 and 0.8 GeV is 15.1±2.3%, assuming a possible 15% uncertainty for the theoretical estimate. This observed consistency between these two independent methods gives us confidence that the corrections made are reliable.

The corrected electron and positron spectra were extrapolated to the top of the atmosphere (ToA) by solving simultaneously the cascade equations describing the propagation of electrons, positrons and gamma rays that result from bremsstrahlung of the electron component. From this, we obtained the positron to electron ratios that are shown in Table 2 along with the median energy at the top of the atmosphere.

The resulting positron to electron ratio is plotted in Fig. 6 together with previous measurements (Fanselow et al. 1969, Daugherty et al. 1975, Muller and Tang

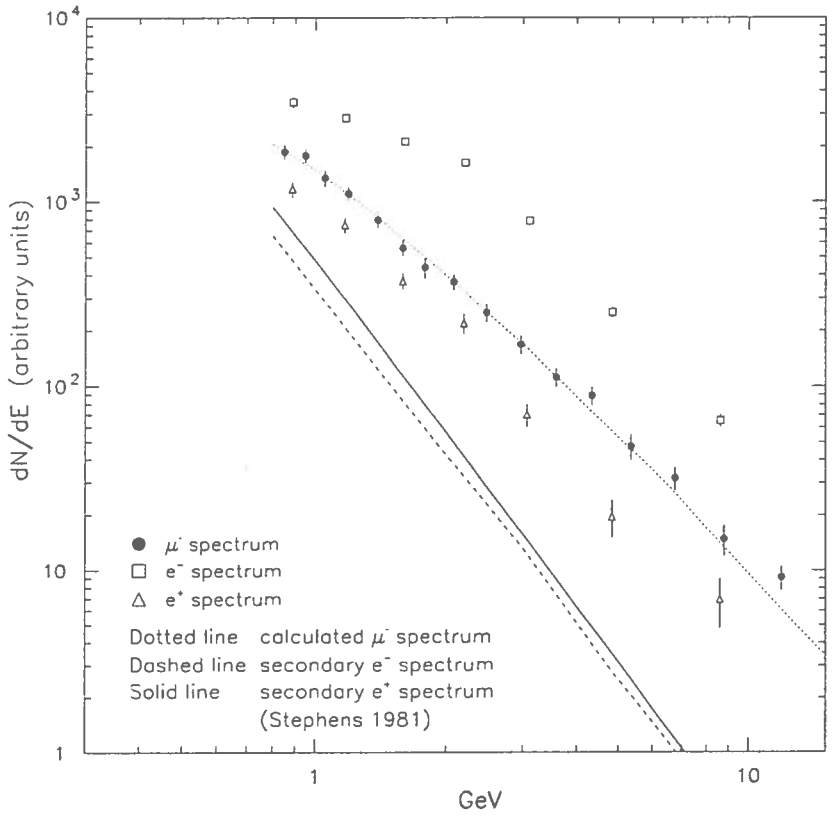

Figure 5: The measured electron and positron flux at the top of the payload, the analytically determined atmospheric background, and the measured muon spectrum with an analytical prediction.

1987, Golden et al. 1987, Golden et al. 1994, Barwick et al. 1995, Golden et al. 1996, Agrinier et al. 1969, Clem et al. 1995). The errors shown includes both the statistical and the systematic errors. Our results are in agreement with the recent measurements (Golden et al. 1996, Barwick et al. 1995) at the upper energy bins. The positron fraction (R) decreases from 0.14 at 0.8 GeV to 0.075 at 4 GeV and remains nearly constant above this energy. The observed energy dependence of the CAPRICE results is consistent with that expected from the simple leaky box model (Protheroe 1982). The value of the ratio is dependent on the amount of matter traversed in the interstellar space and on the assumed spectrum of electrons; both these have large uncertainties. It is essential to obtain the absolute spectra of both electrons and positrons to derive useful information on the origin and propagation of these components. The analysis to obtain absolute fluxes of electrons and positrons is in progress as well as efforts to extend the analysis to lower energies.

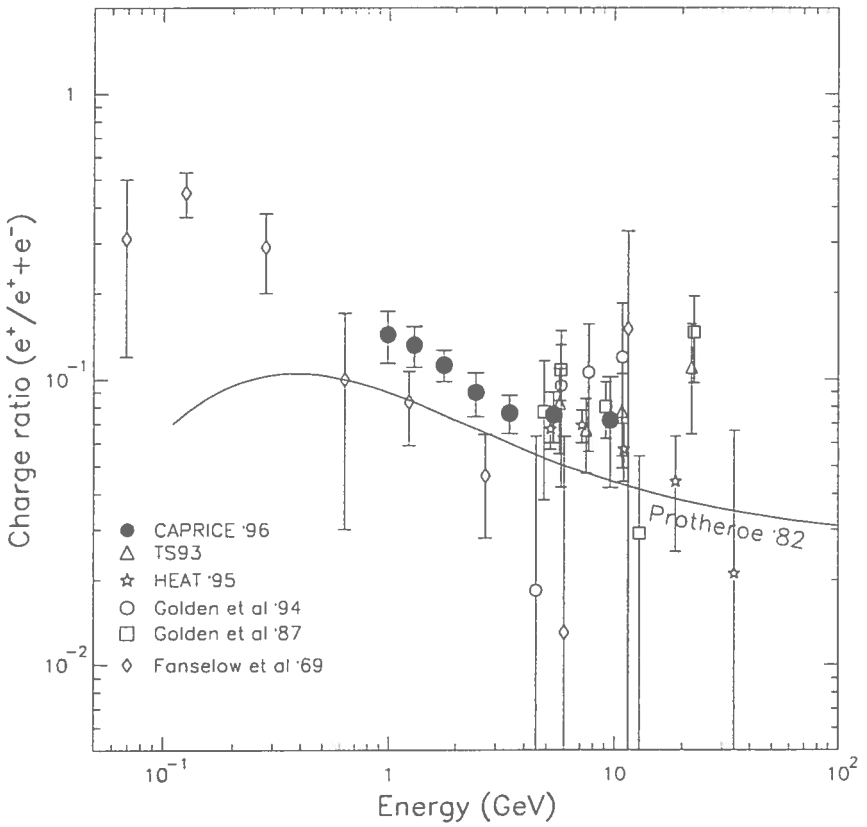

Figure 6: Positron fraction $e^+ / (e^+ + e^-)$ as observed in this experiment compared with other published data and a simple leaky box model.

3 The cosmic ray antiproton flux.

Antiproton search started long time ago following an original idea of L. Alvarez that suggested the possibility of flying a magnetic spectrometer using superconducting coils.

Due to the small amount of $\overline{p}$ in CR ($\overline{p}$ /p *sim* 10^{-4}) and because of the large electron background the progress in this field of CR has been quite low in the past.

Recent balloon missions using the most advanced techniques developed in the particles accellerators have improved substantially the experimental status of the art.

But for most relevant progress the future space based missions are strongly needed.

Data from two balloon flight collaboration (CAPRICE, BESS) will be reported in the following.

Table 3: Summary of proton - antiproton results.

Rigidity at spectrometer GV/c	Observed number of events[a] $\bar{p}$	p	Extrapolated number at top of payload $\bar{p}$	p	Atmospheric correction $\bar{p}$	p	$\frac{\bar{p}}{p}$ at TOA[b]
1.2 - 2.8	4(1)	124658	8.6	303433	1.5	8484	2.5 (+3.2,-1.9) $\times 10^{-5}$
2.8 - 4.0	5(0.7)	25260	17.7	90451	1.4	1662	1.9 (+1.6,-1.0) $\times 10^{-4}$

[a]The numbers shown in the brackets are the estimated muon, pion and electron background.
[b]Top of the Atmosphere. The quoted errors are a combination of statistical and systematic errors.

3.1 CAPRICE FLIGHT 94 for $\bar{p}$ search

The NMSU-Wizard/CAPRICE spectrometer described previously for the e^+ data has also collected $\bar{p}$ data.

For this data the 50 $\times$ 50 cm^2 RICH detector (Carlson et al, 1994) is essential other equipment like time of flight and imaging calorimeter support the antiproton signal amoung the more copious negative particles e^- , μ^- , ...

3.1.1 Data analysis

The analysis was based on 18 hours of data collection for a total acquisition time of 60520 seconds under an average residual atmosphere of 4 g/cm^2.

The data analysis must use the information available from the different detectors to safely identify the antiprotons in a very large background of other particles. Albedo particles, as well as the large number of protons and electrons, must be rejected in the antiproton analysis. About 4% of the cosmic ray protons interact in the atmosphere above the spectrometer and produce π^- and μ^- that must be rejected. Interactions in the spectrometer and associated bar structure also results in a background of negatively charged particles. The remaining background in the antiproton sample is carefully estimated using experimental data and simulations. The selection of protons is more straightforward with little background to reject.

Based on the ability of the RICH to reliably identify antiprotons from pions, muons and electrons, the rigidity range chosen for our analysis was 1.2 to 4.0 GV/c. This rigidity bin was divided into two: 1.2 to 2.8 GV/c and 2.8 to 4.0 GV/c. At 1.2 GV/c the RICH (anti)proton selection efficiency becomes higher than 50%. At a rigidity of 2.8 GV/c, the Cherenkov angle of (anti)protons becomes less than six standard deviations away from the Cherenkov angle of the β (velocity) $\sim$ 1 particles (pi-

Table 4: Antiproton and proton fluxes at the top of the atmosphere.

Kinetic Energy at TOA[a] GeV	Geometrical factor $(m^2\ sr)^{-1}$	Antiproton flux at TOA[b] $(m^2\ sr\ s\ GeV)^{-1}$	Proton flux at TOA[b] $(m^2\ sr\ s\ GeV)^{-1}$
0.6 - 2.0	179.1 ± 2.8	1.9 (+2.4, -1.4) $\times 10^{-2}$	743 ± 17
2.0 - 3.2	177.5 ± 2.8	5.3 (+4.5, -2.9) $\times 10^{-2}$	278 ± 10

[a]Top of the Atmosphere.

[b]The quoted errors are a combination of statistical and systematic errors.

ons, muons and electrons). 4 GV/c is the rigidity where the (anti)proton Cherenkov angle becomes less than three standard deviations away from the Cherenkov angle of $\beta \sim 1$ particles.

For the first time, the combination of an electromagnetic calorimeter and a ring imaging Cherenkov detector has been used to measure the cosmic ray flux of antiprotons. This combination has made it possible to accurately identify antiprotons in the presence of a large background of lighter, negatively charge particles. It also allows an accurate determination of the contamination within the antiproton sample.

The flux of antiprotons and the ratio of antiprotons to protons increase over the kinetic energy interval 0.6 to 3.2 GeV. In agreement with other recent data (e.g. Mitchell et al. 1996), it supports the conjecture that the antiprotons in this energy range are produced in the interstellar medium by primary cosmic rays colliding with interstellar gas.

The combination of all available data on the ratio in the energy range 0.3 to 3 GeV (Moiseev et al. 1996, Bogomolov et al. 1987 & 1990, Mitchell et al. 1996, and this work), shows an increase with energy in agreement with calculations by Gaisser and Schaefer (1992). However, the combined data do not rule out a faster increase than calculated. The two measurements that have been reported above 4 GeV by Golden et al. (1984) and by the MASS91 experiment (Hof et al. 1996) differ by about three standard deviations and further measurements are clearly needed in order to rule out any exotic antiproton production. Fortunately, new experiments are in progress.

3.2 Selection criteria to identify $\overline{p}$

3.2.1 Scintillators

Particles with charge one were selected using the measured energy loss in the top scintillator. From the observed distribution of the dE/dX as a function of rigidity,

singly charged proton like events were selected in the following manner.

3.2.2 RICH

The RICH was used to measure the Cherenkov angle of the particle and thereby its velocity. The velocity and incidence angle dependent Cherenkov angle resolution were determined using a large number of protons selected by the calorimeter and the scintillators. The resolution varied from 8 mrad (perpendicular incidence and $\beta \sim 1$) to about 23 mrad (10° off perpendicular incidence and $\beta = 0.78$). Since the RICH is the only detector capable of clearly identifying antiprotons against a background of muons, pions and electrons in the rigidity range 1.2 to 4 GV/c, strict cuts were applied on the RICH data. A good agreement between the particle's impact position as determined by the RICH and the tracking system was required. The difference in x and y should be less than three standard deviations (rigidity dependent), typically < 5 mm. Using these conditions, reliable Cherenkov angle information was obtained.

3.2.3 Calorimeter

The calorimeter was used to identify electromagnetic showers. The longitudinal and transverse segmentation of the calorimeter combined with the measurement of the energy lost by the particle in each silicon strip resulted in high identification power ($\sim 85\%$) for electromagnetic showers combined with a high rejection power ($\sim 10^4$) for hadronic particles (Barbiellini et al. 1996). In the analysis presented in this paper, the calorimeter was used to reject events with electromagnetic showers initiated by a single electron, possibly accompanied by a bremsstrahlung photon emitted in the RICH or in the dome above the detector stack (see Weber 1996 for a description of the selection criteria).

Figures 7 and 8 illustrate the calorimeter performance, and show schematic views of two single events in the CAPRICE apparatus. The instrument is shown in the bending (x) view and in the non-bending (y) view. From top to bottom is displayed: the RICH seen from above, the tracking stack of multiwire proportional chambers and drift chambers, and the imaging calorimeter. Note that Figures 7 and 8 are not to scale; the calorimeter is significantly thinner than shown in the figure. Figure 7 shows a single 1.3 GV/c electron traversing the apparatus and emitting a bremsstrahlung photon in the RICH. The RICH shows the detected Cherenkov light image where the ionization of the chamber gas by the electron is shown as a cluster of pads hit in the centre surrounded by the signals from the Cherenkov light. Due to total reflection in the NaF crystals, only part of the Cherenkov ring is

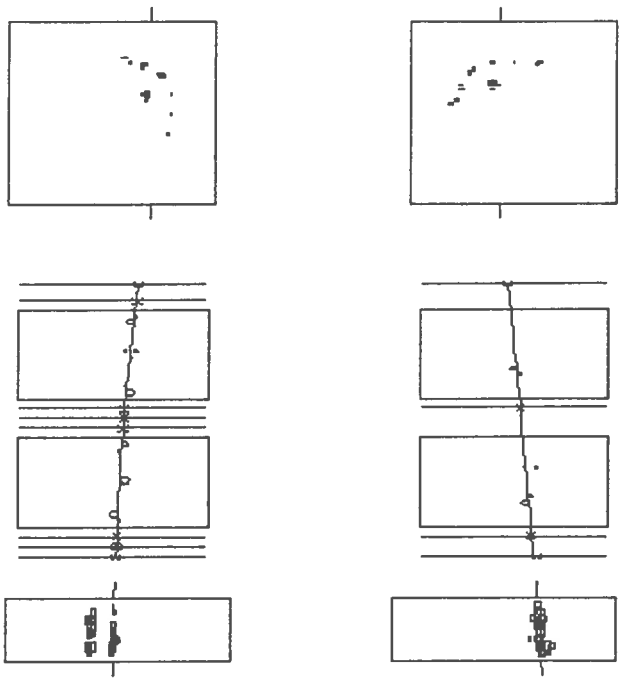

Figure 7: Display of a single 2.2 GV antiproton traversing the CAPRICE apparatus. The antiproton interacts in the calorimeter showing clearly several charged particles emerging from the vertex of interaction; this could be an annihilation in flight.

detected. The tracking stack shows the trajectory of the electron as it is deflected by the strong magnetic field. The calorimeter shows the two electromagnetic showers produced by the electron and the bremsstrahlung photon, respectively. The origin of the bremsstrahlung photon can be located by projecting backward the direction of the shower and determining where it intersects the electron trajectory. More than one fourth of the electrons in the rigidity region 1.2 to 4 GV/c were accompanied by a bremsstrahlung photon reconstructed in the calorimeter.

Similarly, Figure 8 shows a single 2.2 GV/c antiproton traversing the instrument. The ring of Cherenkov light is clearly seen in the RICH, giving an accurate velocity determination for the particle. The rigidity is measured from the deflection in the tracking system. The antiproton interacts in the calorimeter, clearly showing many charged particles emerging from the vertex of interaction; this could be an in-flight annihilation. The interaction probability for a 2.2 GV/c antiproton is about 40%.

3.2.4 Tracking

The tracking information must be carefully used to eliminate positively charged particles (protons), that have scattered in the tracking system and therefore look like negatively charged particles. Events with more than one track also must be

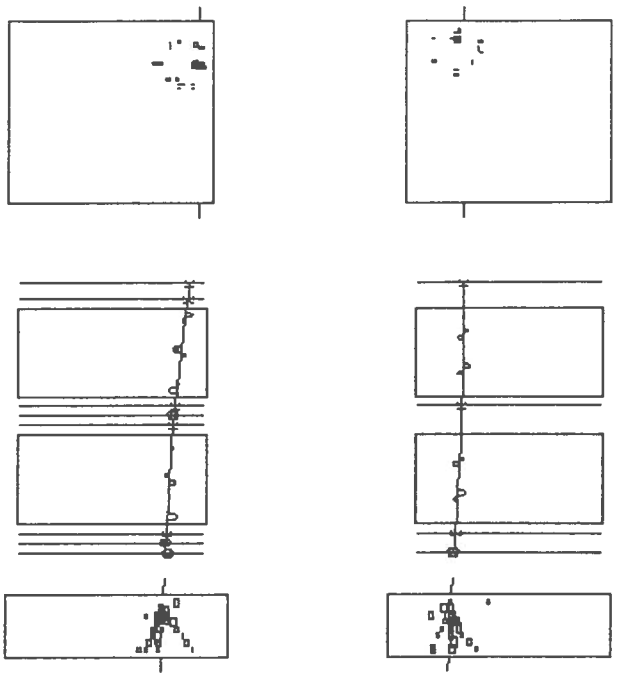

Figure 8: Display of a single 2.2 GV antiproton traversing the CAPRICE apparatus. The antiproton interacts in the calorimeter showing clearly several charged particles emerging from the vertex of interaction; this could be an annihilation in flight.

eliminated. To achieve this goal, a set of conditions were imposed on the fitted tracks. These conditions represent a compromise between rejection power and efficiency and are partly based on experience gained previously using the same tracking system (Mitchell J. et al. 1996, Hof M. et al. 1996).

4 BESS-93 to BESS-95 FLIGHTS

The largest sample of $\overline{p}$ in CR collected so far is the one obtained by the magnetic spectrometer built by the BESS collaboration.

The BESS experiment has been carried out as a joint research project University of Tokyo, National Laboratory for High Energy Physics (KEK), Kobe University, Institute of Space and Astronautical Science (ISAS) in Japan and National Aeronautics and Space Administration (NASA), New Mexico State University (NMSU) and University of Maryland in the United State to search for cosmic ray antiparticles and to make precise measurements of cosmic ray spectra.

The BESS spectrometer had been developed since 1987, and three successful scientific flight have been carried out in Canada since 1993.

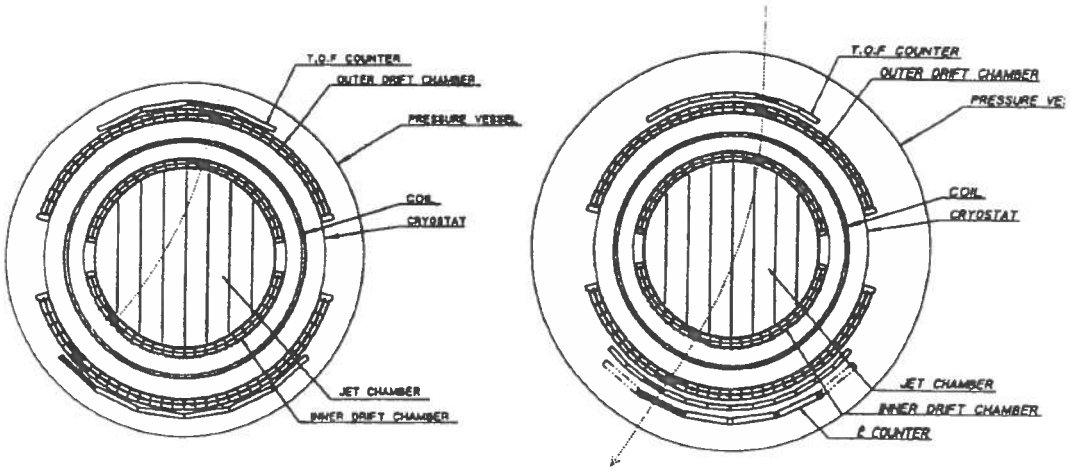

Figure 9: Cross sections of BESS spectrometer

4.1 BESS spectrometer and flights

Figure 9 show cross sections of the BESS spectrometer. The first two flights were made with the configuration (a) and the third flight in 1995 was carried out with the configuration (b) after the up-grade of TOF counters with a new pressure vessel. Table 5 gives the latest major spectrometer parameters.

Table 5: Main parameters of BESS Spectrometer (II)

Geometrical Acceptance	0.4 m^2sr
Maximum Detectable Momentum	200 GeV/c
Momentum Region for Antiproton search	2 GeV/c ($\gg$ 3 GeV/c)
Momentum Region for Anti-helium search	50 GeV/c
Trigger Rate	1 - 2 kHz
Event Recording Rate	100 - 200 Hz
Sensitivity for Antiparticle Search	10^{-6} - 10^{-7} / one day flight
Trasparency of Half Detector Wall	7.5 g/cm^2
Size of Pressure Vessel	1.7 m$\oslash$ $\times$ 3.6 m
Weight of Payload	2.2 ton
Power Consumption	1.2 kW

The BESS spectrometer was launched by using 29 MCF balloons, in summers since 1993.

4.2 Summary and further improvements for future flights

The BESS spectrometer has detected more than 40 low energy antiprotons with precise energy measurement, and has resulted the upper limit of antihelium to helium ratio down to 2×10^{-6}.

Figures 10 and 11 show the BESS-93 results on the $\bar{p}$ flux and the $\bar{p}$ /p ratio. By an important improvement on the TOF the BESS-95 flight has enlarged the momentum internal on the $\bar{p}$ increasing consequently the statistic avaiable on the world $\bar{p}$ sample.

Figure 12 shows the clean $\bar{p}$ sample in the plat $1/\beta$ versus rigidity (β is the $\bar{p}$ velocity in unit of c).

Figure 13 and Table 6 give the results on the $\bar{p}$ flux in 5 and 4 energy bins.

Table 6: Results of 1995 flight

Energy, MeV	$\bar{p}$ /p ratio	Antiproton flux
200-500	1.3×10^{-5}	0.016
500-700	1.2×10^{-5}	0.013
700-1000	1.6×10^{-5}	0.012
1000-1200	3.3×10^{-5}	0.019

4.3 BESS search for the antihelium

All helium events were carefully checked for an antihelium. Event # 1,656,905 from 95 flight showed good parameters but unfortunately had not good consistency of Z coordinate measured by TOF and by tracking system and had a sign of interaction above upper IDC. It does not allow us to accept this event as the first detected non-hydrogen antinucleus.

The BESS collaboration has computed an $\overline{He}$ limit on the basis of the data from 93-94 data.

The presence of the $\overline{He}$ in the cosmic ray would be an important discovery implying the existence of primary antimatter with Universe.

The figure 14 shows the rigidity distribution of the detected cosmic rays. From the absence of candidate with negative charge the limit shown in the following figure is derived. BESS is planning an infrared detector flight in the 97 and possible long duration flights in the 99 and later.

The expected $\bar{p}$ results from the future activity are shown in the following figures. A very comprehensive presentation of the BESS results are pubblished in the

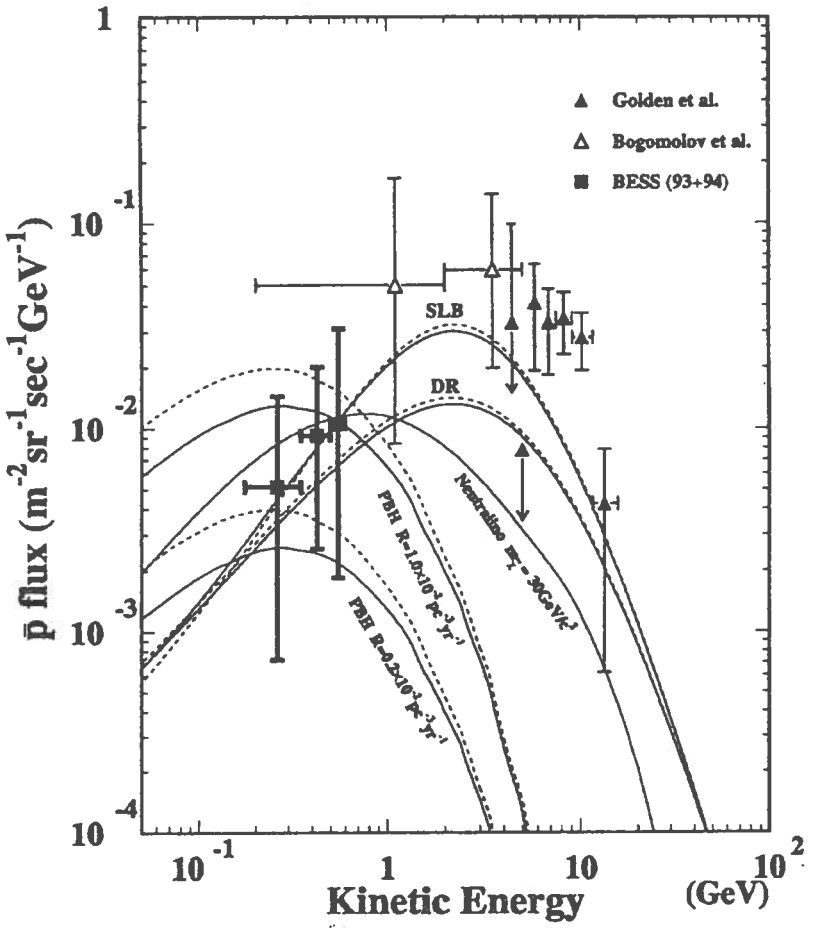

Figure 10: Measured $\bar{p}$ flux in comparision with the results of other experiments and calculations. Filled squares, the present results; filled triangles, Golgen et al.; open triangles, Bogomolov et al.. The curves labeled "SLB" and "DR" are recently calculated by Mitsui based on Standard Leaky Box Model and Diffusive REacceleration Model, respectively. The dashed curves are for the minimum solar modulation and the solid are for $\phi = 600$ MV. The curves labeled "PBH are calculations by Maki et al. on the $\bar{p}$ production by Primordial Black Holes for two values of evaporation rate R. The dashed and solid curves again for the minimum and $\phi = 600$ MV solar modulations. The curve labeled "Neutralino is calculated by multiplying the model of the proton flux and the $\bar{p}$ /p ratio by Jungman and Kamionkowski based on the $\bar{p}$ production by annihilations dark matter neutralinos.

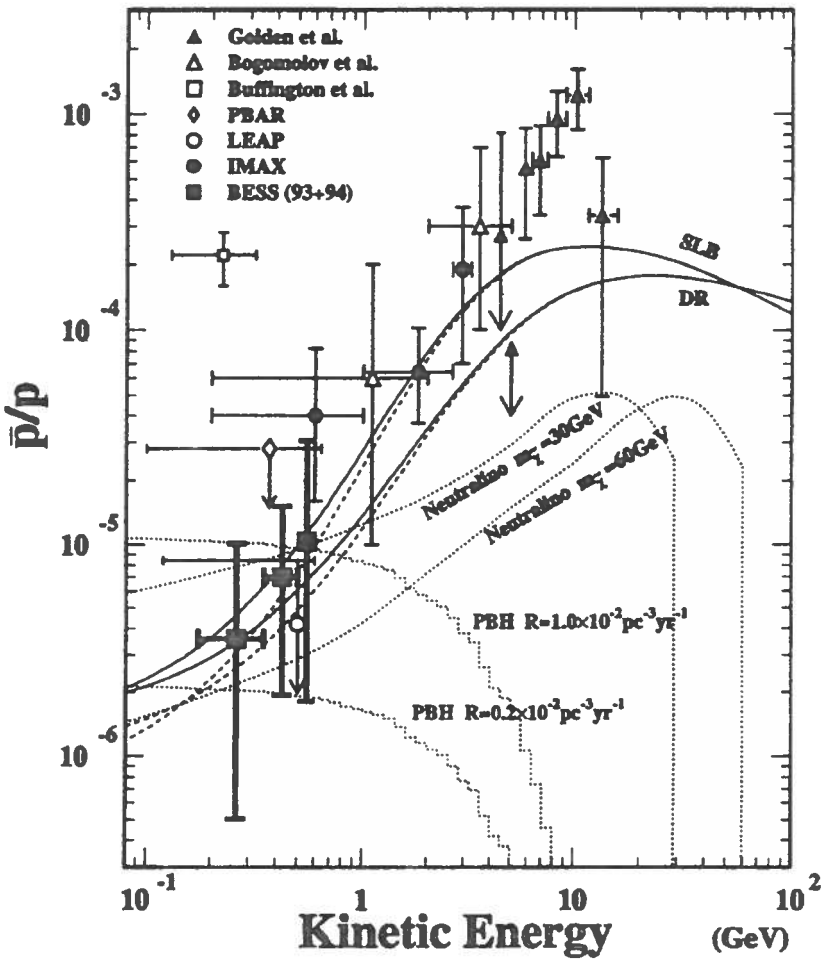

Figure 11: Measured $\bar{p}$ /p ratio in comparision with the other experimental data and calculations. Filled squares, the present result; filled triangles, Golden et al.; open triangles, Bogomolov et al.; open square, Buffinton et al.; open diamond, the PBAR experiment; open circles, the LEAP experiment; filled circles, the recent result of IMAX. The dashed curves labeled "SLB" and "DR" are recently calculated by Mitsui based on based on Standard Leaky Box Model and Diffusive REacceleration Model, respectively. The dotted curves labeled "PBH" are prediction of MAKI et al. for the $\bar{p}$'s produced by primordial black holes with two different assumed evaporation rates R. The dotted lines labeled "Neutralino" are the prediction of Jungman and Kamionkowski for the $\bar{p}$ productions by annihilations of dark matter neutralinos.

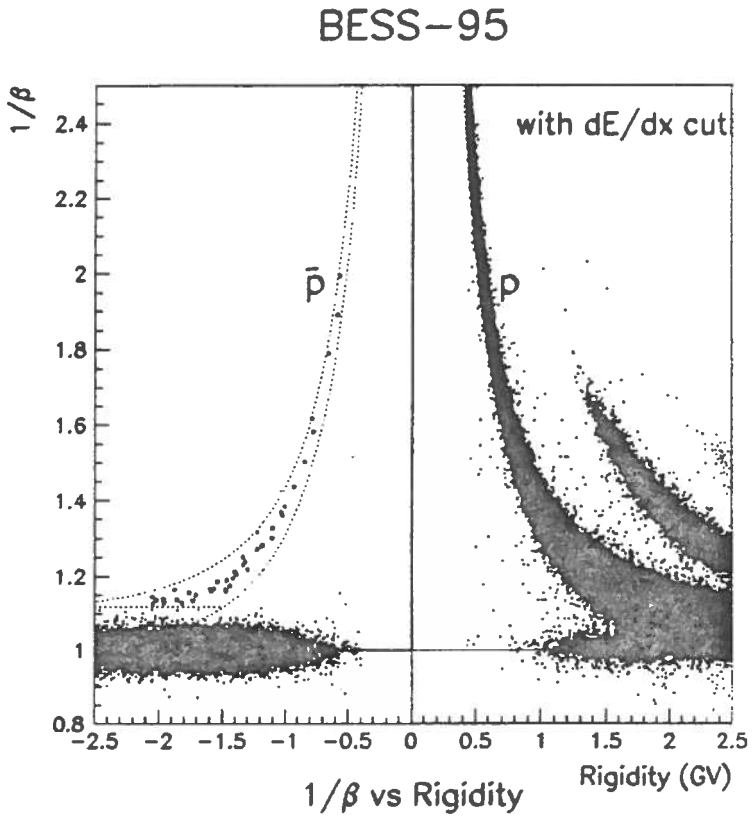

Figure 12: The identification of antiproton events after dE/dx cut. The antiproton events are marked as $*$.

Proceedings of the 6^{th} Workshop on BESS pubblished as KEK Proceedings 96-9.

4.4 Future

The BESS long duration flights expectation show an impressing improvement on the experimental Knowledge of antimatter with CR. But the most important step forward is expected to come from future space experiments. Long duration in this case means more than three years, so statistic can increase largely even with effective area of reduced dimension.

But probably the experiments on space will improve the experimental situation because there is not residual atmosphere on top of the detector that introduce an unavoidable background in so reliably computed.

Two projects on antimatter search in space are in a stage of advanced construction. The basic principle are similar using both as basic element a magnetic spectrometer with permanent magnet to give the magnetic field inside a region where high space accuracy tracker (Si tracker) are inserted. The basic elements of the two experiments are implemented in different ways by particles identification detectors.

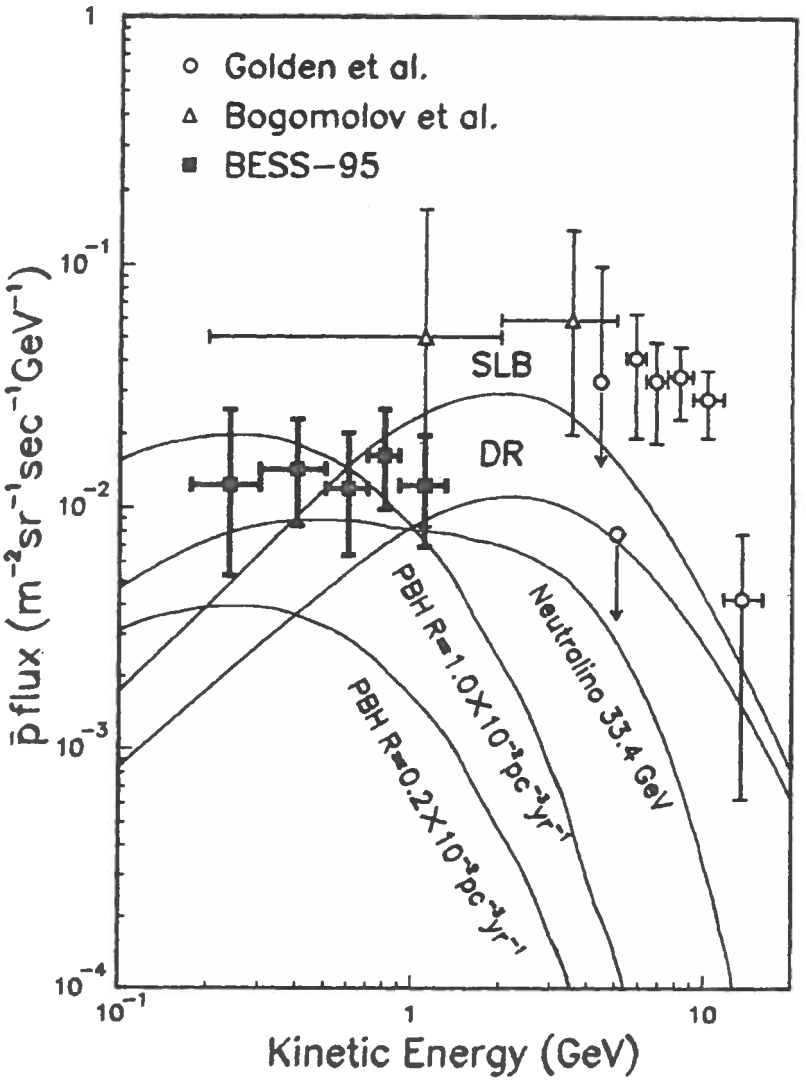

Figure 13: Comparision of the measured $\bar{p}$ flux with the other experiments and theoretical values. Filled square, the present result; open circle, Golden et al.; open triangle, Bogolomov et al.. The curves labeled "SLB" and "DR" are calculated by Mitsui based on Standard Leaky Box Model and Diffusive Reacceleration Model, respectively. The curves labeled "PBH" are calculated by Maki et al. for the $\bar{p}$ production by Primordial Black Holes. The curve labeled "Neutralino" is calculated by Jungman and Kamionkowski based on the $\bar{p}$ productions by annihilations of dark matter neutralinos.

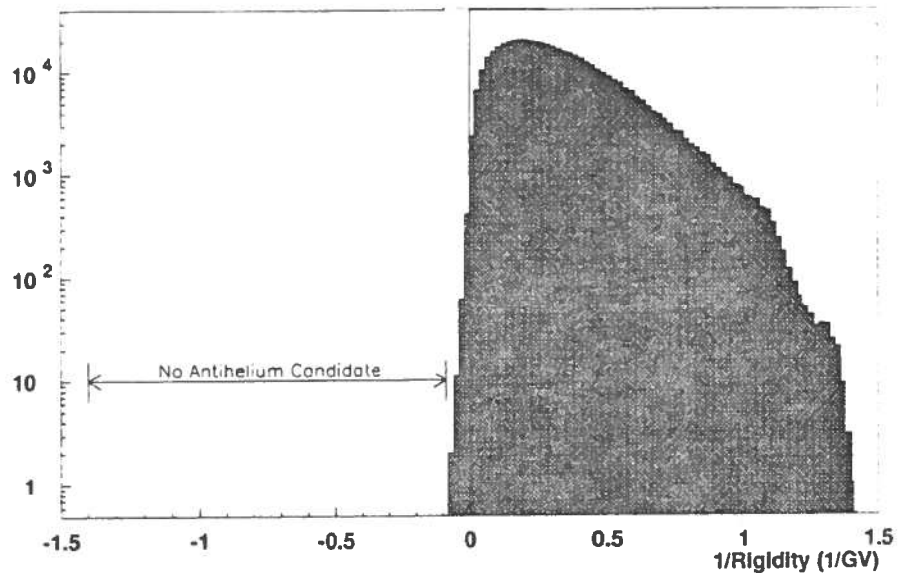

Figure 14: 1/Rigidity distribution.

The AMS spectrometer will be located in the International Space Station Alpha (ISSA) after a flight test in the Shuttle scheduled in the 1998.

In the figures 16 and 17 is shown a schematic of the AMS detector. The location of the AMS detector on the Shuttle and on the space station (ISSA).

Figure 18 show the expected improvement of the antimatter/matter ratio obtained by AMS after 3 years running on ISSA.

5 Pamela

Pamela is part of the Russian Italian Mission (RIM) program a collaboration between INFN and the VNIIEM institute of Moscow with partecipation of other international institutes, for sending in space cosmic ray telescopes as "piggy-back" in someone of their satellites of the Resurs series.

The opportunity is unique both for thr very favourable attitude of these satellites (looking to the Earth surface, and indeed out of the Earth on the other side) and for their polar orbit, allowing to cover the whole energy range down to very low energies, highly enriching the possible physics program. Furthermore their orbit is quasi circular at about 700 km, what garantees a very long permanence in flight, ad sun-syncronous, what maximizes the electric power availability.

The group of Prof. Arkady Galper, of the MEPI of Moscow, acted as interface with the VNIIEM institute, so that in '93 it was elaborated a Russian Italian Mission (RIM) program, of what the RIM-2 experiment, that we named PAMELA, is the

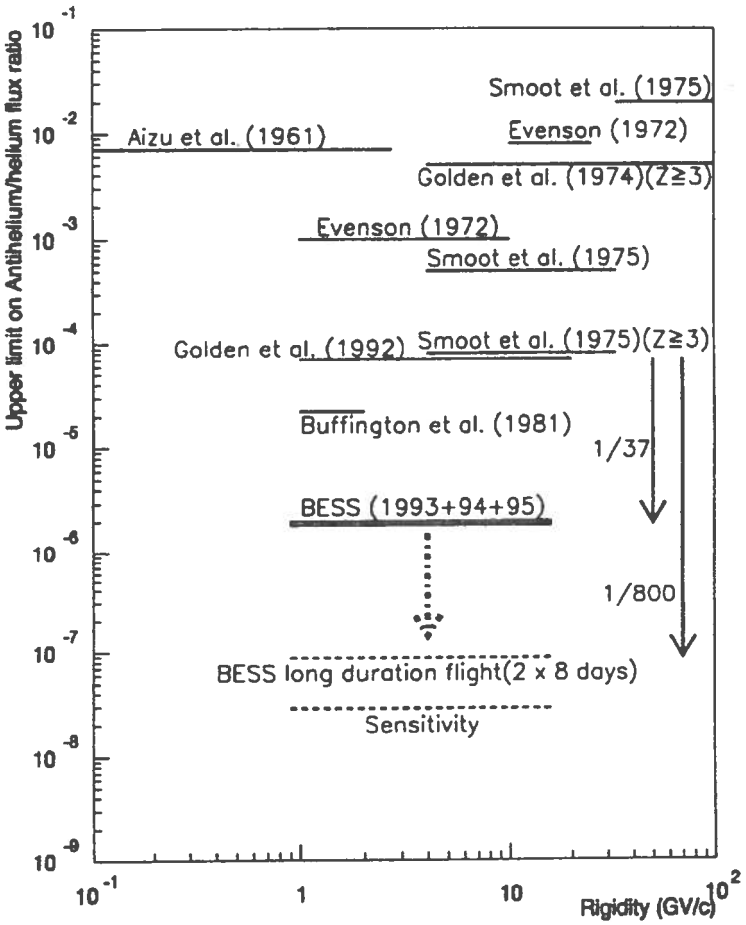

Figure 15: Upper limit on $\overline{\text{He}}$/He flux ratio.

central part.

5.1 The technical choices and the baseline design

The relative low magnetic field intensity due to use of a permanent magnet can be compensated with the progress made in the recent years in particle localization by the wide application of the silicon microstrip detectors.

The tests made in '94 and '95 of prototypes of the foreseen sensors for the PAMELA tracker guarantee the successful handling of this difficult technique.

The chosen cross section of the magnet gap is 14 × 16 cm^2, macthing the optimal use of the 4 inch silicon wafers to produce large area silicon microstrip sensors. For maximizing the MDR we chose to have a relatively weak field (~0.35 T) on a relatively long magnetic path (44 cm, nearly the maximum allowed by the geometrical constraints to the experiment). The corresponding MDR is ~ 370 GV/c. The magnetic gap and the magnet length determine the angular acceptance of the

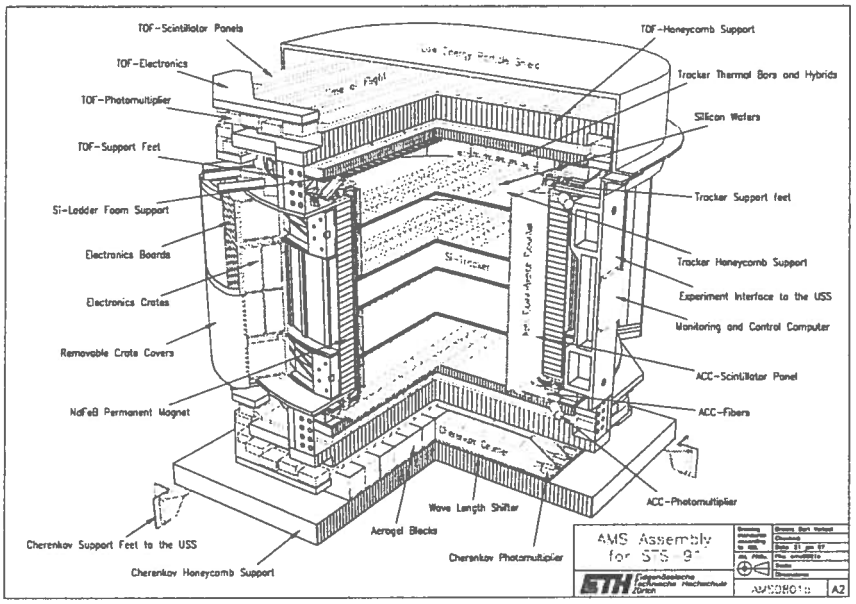

Figure 16:

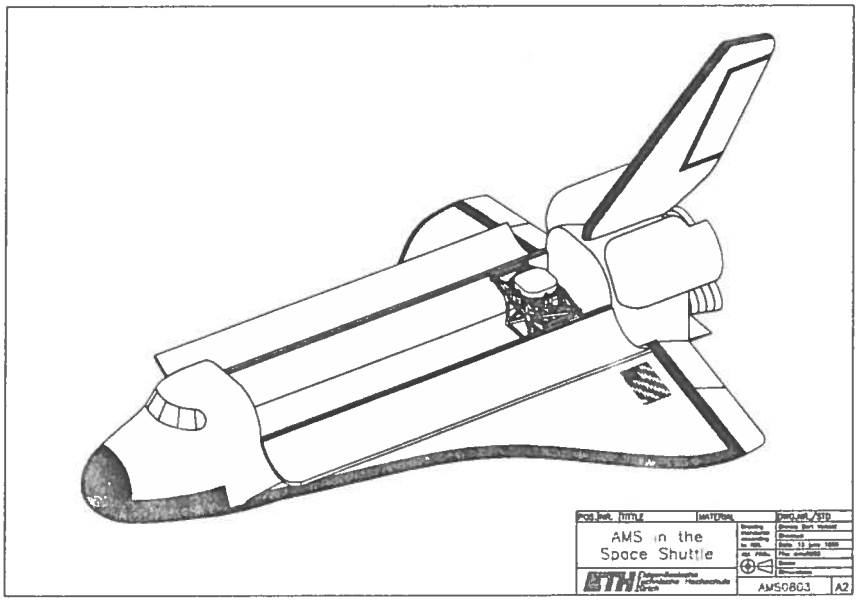

Figure 17:

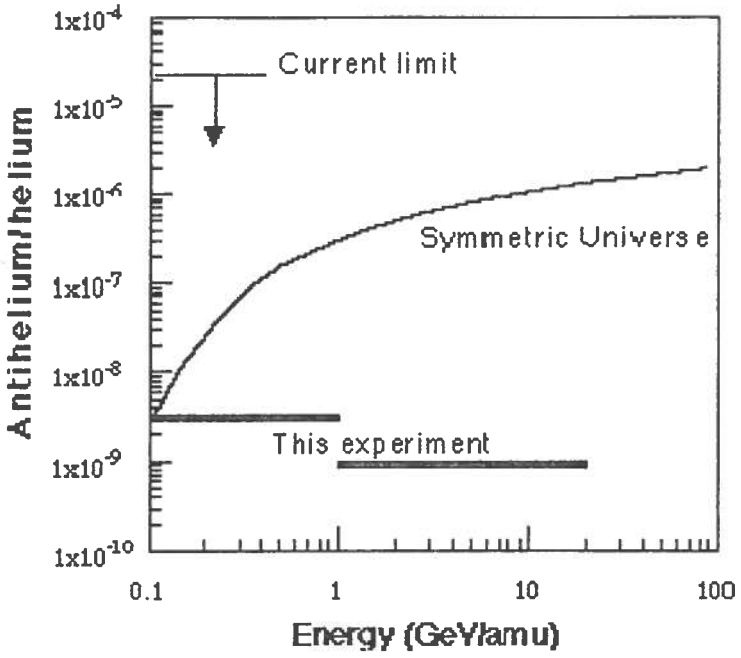

Figure 18:

telescope, 20. $0^o \times 17.7^o$, to which corresponds the geometrical acceptance of 24.5 cm^2 sr.

At low momenta it is dominated by the multiple scattering of the particle in the silicon sensors and in their supporting structures, afterward it increases linearly with the momentum.

The antiproton counting rate in the given GF is reported in figure 19 in two hypotheses: 1) only secondary produced antiprotons according to the Modified Leaky Box Model of the Galaxy (lower curve); 2) only secondary produced antiprotons according to the Closed Galaxy Model (CGM). Any primary production mechanism will increase these rates. the counting rate foreseen for the positrons is reported in figure 20.

The technical choices for the other detectors are the following:

- silicon microstrip sensors for the imaging calorimeter, interleaved with tungsten plates as assorber; this choice minimizes the volume of the calorimeter, and maximizes indeed his geometrical acceptance; the high granularity assumed in PAMELA allows a very good separation between electromagnetic showers and interacting or not interacting hadrons; the chosen depth allows a good resolution in the measurement of the energy of electromagnetic particles, further extending the energy spectrum measurements of electrons and positrons;
- several scintillation counter hodoscopes for the costruction of the triggers and for the TOF measurements; the use of several hodoscope allows independent

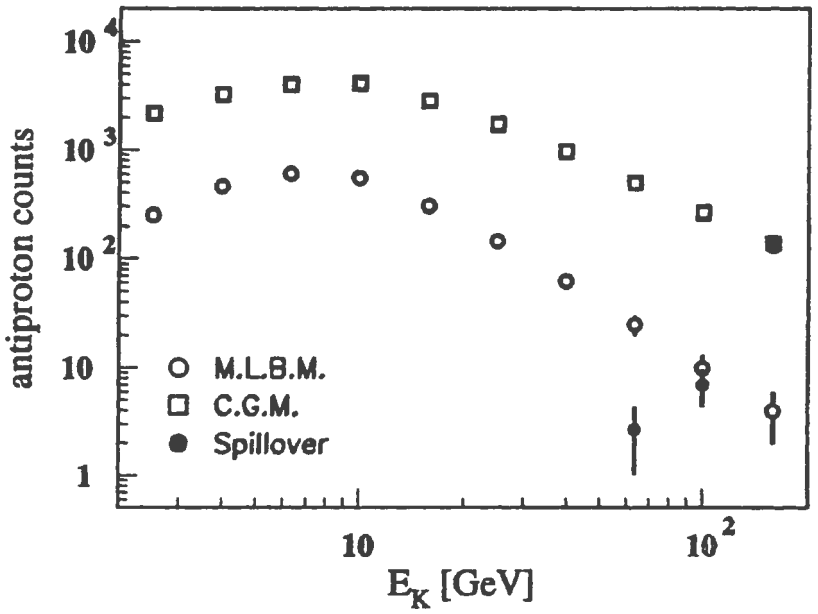

Figure 19:

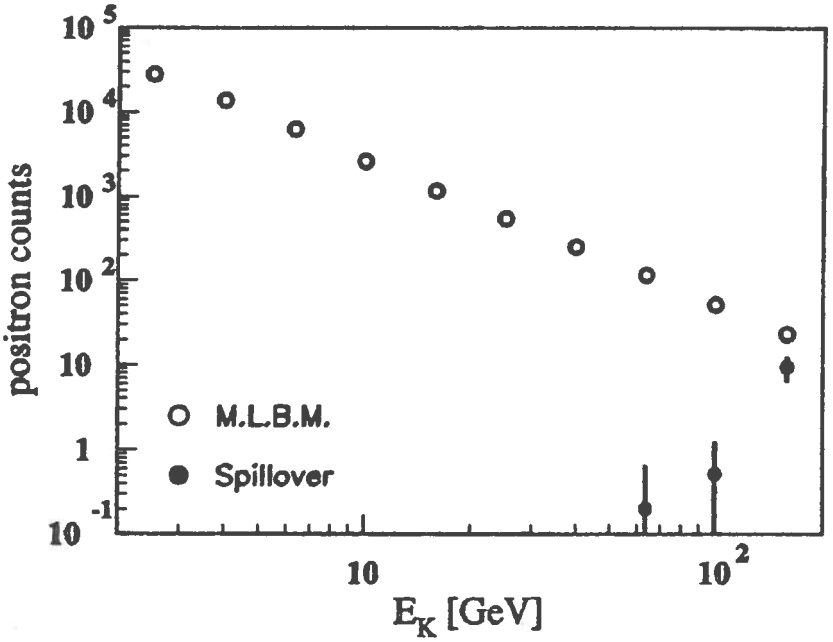

Figure 20:

TOF measurements, improving the precision and the safety; the hodoscope structure maximizes the yield of the collected light and the safety of the system; both the hodoscopization and the number of hodoscopes allow a good flexibility in constructing the first level triggers.

- a Transition Radiation Detector (TRD) for selecting electromagnetic particles from hadrons up to very high energy (~1000 GeV); the TRD is based on small diameter straw tubes arranged in double layer planes interleaved by carbon fiber radiator. The use of the straw tubes allows to perform many energy loss measurements along the particle trajectory (what brings down to less than 1 GeV the selection capability of the instrument), and to track all particles before their entrance in the magnetic spectrometer, cleaning the sample of the particles accepted at its entrance;
- a sixth scintillator layer will be located below the calorimeter as a penetration detector;
- finally a set of scintillation counters covering the top edge and the sides of the magnetic spectrometer completes the telescope, for a further labelling of contaminated events.

The PAMELA telescope (see figure 21) consists of the following subdetectors (from the top to the bottom):

- two scintilllation counter hodoscopes (S11 and S12);
- the TRD counter, occupying 29 cm in height;
- one scintillation counter hodoscope (CAT) on the top of the magnet, labelling the particles not entering the magnet gap;
- the magnet + tracker system, consisting of 5 permanent magnets, each 8 cm high, interleaving 6 detection planes of the silicon microstrip tracker, each 0.8 cm high, the whole closed in a ferromagnetic screen, 0.2 cm thick, and surrounded on its sides by a system of scintillation counters (CAS) labelling the particles entering the spectrometer from the sides;
- two scintillation counter hodoscopes (S21 and S22);
- the imaging calorimeter, consisting of 23 planes of silicon microstrip sensors, interleaved by 23 tungsten sheets, whose physical occupancy in height is 19 cm;

The total height of the spectrometer is 113.5 cm. Tables 7 and 8 give technical parameters of PAMELA and the expected rate over the mission time (3 years).

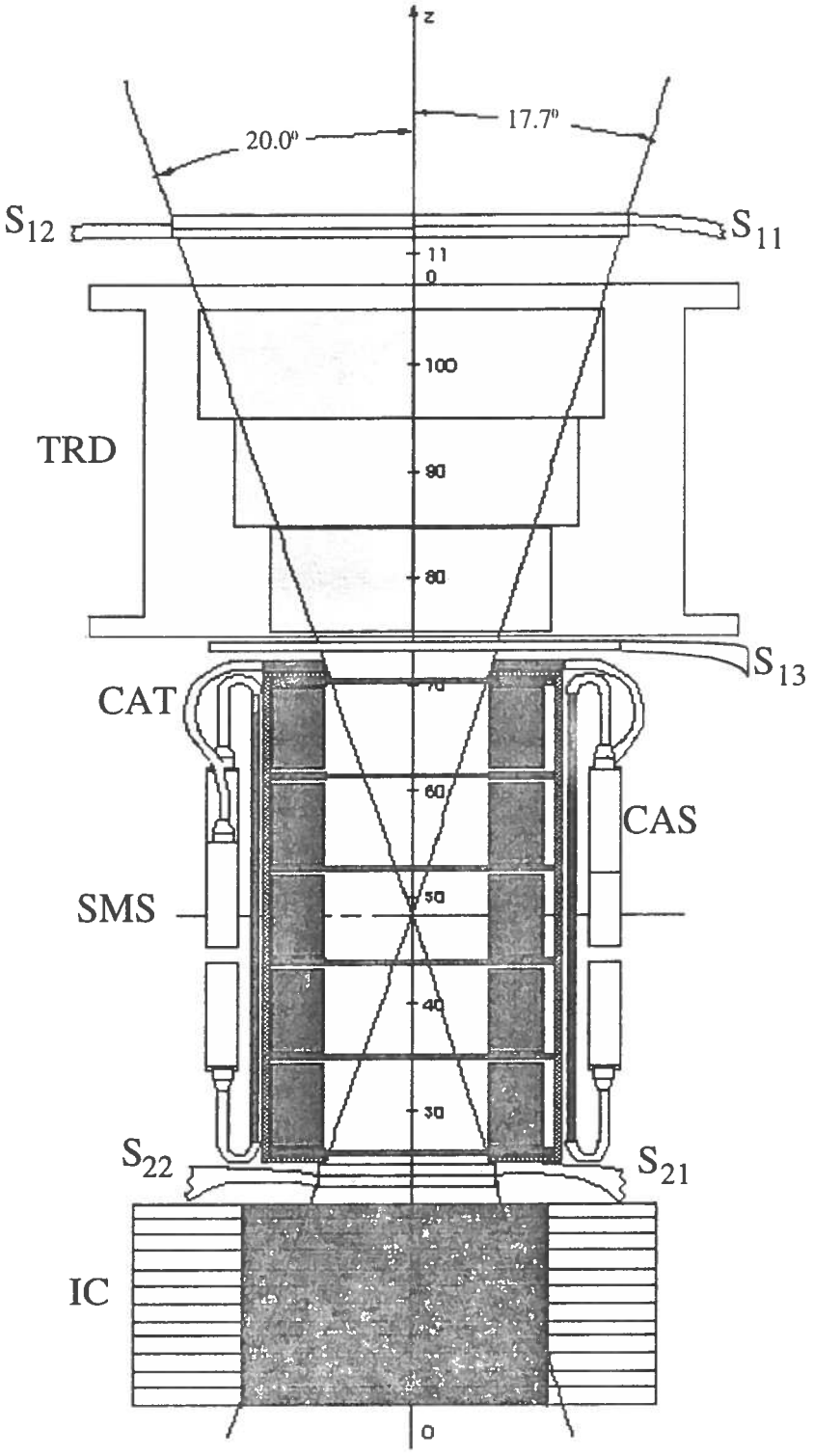

Figure 21: The PAMELA telescope

Table 7: Expected rates in PAMELA in 10^8s

protons	3×10^8
antiprotons	$\geq3\times10^4$
electrons	6×10^6
positrons	$\geq3\times10^5$
He nuclei	4×10^7
Be nuclei	4×10^4
C nuclei	4×10^5
antinuclei limit (90% c.l.)	7×10^{-8}

Table 8: Main parameters of the elements of the PAMELA telescope

	Volume(xyz) (cm × cm × cm)	Mass (kg)	R.O.ch (#)	Power (W)
Scintillation counters	45×40×2 + 17×15×3 + 36×32×1	≤33	34	≤32
Trans. Rad. detector	40×40×29	23	1,920	≤40
Anticoincidences	(21×6×1)×4+ (9×30×1)×15+ (8×30×1)×5+	13	48	≤5
Silicon tracker	(28×24×0.8)×6	10	36,864	37
Imaging calorimeter	30×24×19	129	3,312	≤60
Fast trigger		5		10
General electronics		≤15		25
Power supplay		10		90
Permanent magnet	29×30×47 [(23×24×8)×5+ Fe shielding]	140		
General mechanical structure		25		
Total	45×40×114	≤403	42,178	≤299

6 Conclusion

The progress on our understanding on the presence of antimatter with cosmic rays is recently progressed in a substantial way.

The future improvement will expand our knowledge giving hopefully a conclusive result on the origin of antimatter in the Universe.

Let me conclude this presentation by mentioning that GLAST (show figure 22), the next generation gamma ray (γ) telescope will also contribute to the problem of

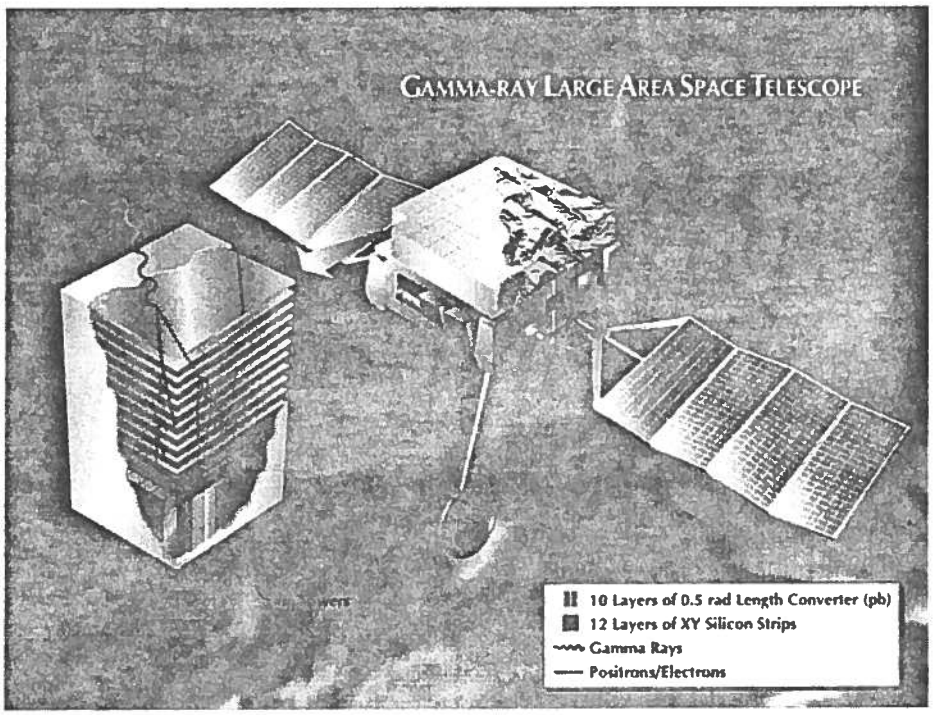

Figure 22:

antimatter search in an indirect way by studing the diffused γ spectrum giving a limit on large scale to presence in the Universe of region where matter antimatter enter in contact and give the typical γ spectrum from π^o decay modulated by the red shift due to the distance from our galaxy of such regions as shown in figure 23, De Rújula A., 1996).

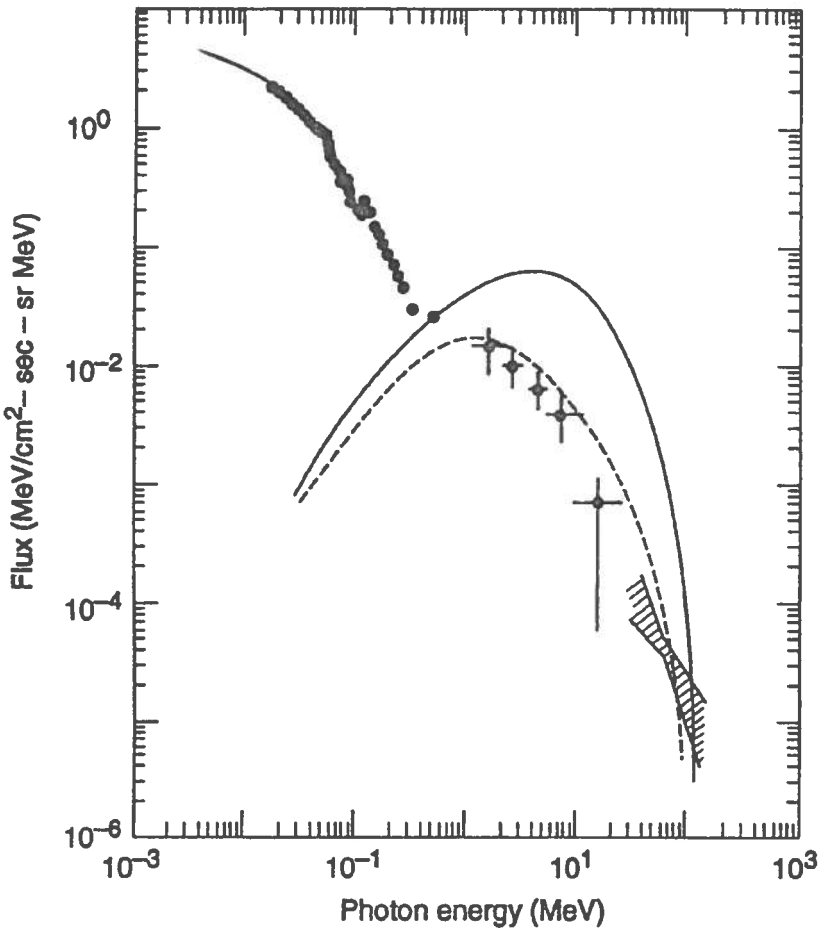

Figure 23: Comparision of the diffuse γ ray energy spectrum with the results of a matter/antimatter symmetric Universe for d = Mpc. Dashed (continuous) lines are with (without) reheating by electrons and positrons from $p\bar{p}$ annihilation.

References

- Adriani, O., et al. 1995, Proc. of XXIV ICRC, Rome, 3, 591
- Agrinier B. et al., 1969, Lett. Nuovo Cimento 1, 153
- Barbiellini, G., et al. 1996a, Nucl. Instr. and Meth., A371, 169
- Barbiellini, G., et al. 1996b, A&A, 309, L15
- Barwick S.W. et al., 1995, Phys. Rev. Lett. 75, 390
- Bocciolini M. et al., 1993, Nucl. Instr. and Meth. A333, 77
- Bocciolini M. et al., 1996, Nucl. Instr. and Meth. A370, 403
- Bogomolov, E. A. et al. 1979, Proc. of XVI ICRC, Kyoto, 1, 330
- Bogomolov, E. A. et al. 1987, Proc. of XX ICRC, Moscow, 2, 72
- Bogomolov, E. A. et al. 1990, Proc. of XX1 ICRC, Adelaide, 3, 288
- Brun, R., et al. 1994, "Detector Description and Simulation Tool", CERN program library
- Buffington, A., Schindler, S. M., & Pennypacker, C. R. 1981, Apj, 248, 1179
- Carlson P. et al., 1994, Nucl. Instr. and Meth. A349, 577
- Carlson P. et al., 1995, To appear in Nucl. Instr. and Meth.
- University of Chicago 1996, National Science Foundation Grant ATM-9420790, http://astro.uchicago.edu/home/web/pyle/neutron.html
- Clem J. et al., 1995, Proc. 24th Int. Cosmic Ray Conf., Rome, Vol. 3, 5
- Daniel R. R. and Stephens S. A., 1974, Rev. Geoph. and Sp. Ph., Vol.12, 233
- Daugherty J. K. et al., 1975, ApJ 198, 493
- De Rújula A., 1996 "Antimatter in the Universe?", CERN program library.
- Fanselow J. L. et al., 1969, ApJ 158, 771
- Gaisser, T. K., & Schaeffer, R. K. 1992, Apj, 394, 174
- Gleeson, L. J., & Axford, W. I. 1968, ApJ, 154, 1011
- Golden, R. L., et al. 1978, Nucl. Instr. and Meth., 148, 179
- Golden, R. L., et al. 1979, Phys. Rev. Lett., 43, 1264
- Golden, R. L., et al. 1984, Astrophys. Lett., 24, 75
- Golden R. L. et al., 1987, A&A 188, 145
- Golden R. L. et al., 1991, Nucl. Instr. and Meth. A306, 366

· Golden R. L. et al., 1994, ApJ 436, 769

· Golden R. L. et al., 1996, ApJ 457, 103

· Hof M. et al., 1994, Nucl. Instr. and Meth. A345, 561

· Hof, M., et al. 1996, Apj, 467, L33

· Kiraly, P., Wdowczyk, J., & Wolfendale, A. 1981, Nature, 293, 120

· Mitchell, J., et al. 1996, Phys. Rev. Lett., 76, 3057

· Mitsui, T., Maki, K., & Orito, S. 1996, "Expected Enhancement of the Primary Antiproton Flux at the Solar Minimum", UT-ICEPP 96-03, 22

· Moiseev, A., et al. 1996, "Cosmic Ray Antiproton Flux in the Energy Range from 200 to 600 MeV", Apj, to appear 1997

· Muller D., & Tang K. K., 1987, ApJ 312, 183

· Papini, P., Grimani, C., & Stephens, S. A. 1996, Il Nuovo Cimento, 19, 367

· Paradis, P. 1996, PhD thesis, New Mexico State University, USA

· Pfeifer, Ch., Roesler, S., & Simon, M. 1996, Phys. Rev. C, 54, 2, 54

· Protheroe R. J., 1982, ApJ 254, 391

· Rudaz, S., & Stecker, F. W. 1988, ApJ, 325, 16

· Silk, J., & Srednicki, M. 1984, Phys. Rev. Lett., 53, 624

· Simon, M., et al. 1996, Apj, 456, 519

· Stecker, F. W., Protheroe, R. J., Kazanas, D. 1981, Proc. of XVII ICRC, Paris, 9, 211

· Stecker, F. W. & Wolfendale, A. W. 1984, Nature, 309, 37

· Stephens S. A., 1981, Proc. 17th Int. Cosmic Ray Conf., Paris, Vol.4, 282, Vol.2, 512

· Stephens, S. A. 1996, "Secondary Antiproton Spectrum in the Atmosphere with the Inclusion of Fermi Motion in Air Nuclei", submitted to Astropart. Phys.

· Sullivan, J. D. 1971, Nucl. Instr. and Meth., 95, 5

· Weber, N. 1996, "A measurement of the antiproton and proton fluxes in the cosmic rays by the CAPRICE experiment" (PhD thesis, KTH Stockholm, Sweden)